UC Davis
UC Davis Previously Published Works

Title

Click-Ready Perfluorocarbon Nanoemulsion for 19F MRI and Multimodal Cellular Detection

Permalink

Journal

ACS Nanoscience Au, 2(2)

ISSN

2694-2496

Authors

Perez, Adam S
Zhou, Junhan
Leach, Benjamin
et al.

Publication Date

2022-04-20

DOI

10.1021/acsnanoscienceau.1c00016

Peer reviewed

Article

Click-Ready Perfluorocarbon Nanoemulsion for ^{19}F MRI and Multimodal Cellular Detection

Adam S. Perez,[∇] Junhan Zhou,[∇] Benjamin Leach, Hongyan Xu, Deanne Lister, Stephen R. Adams, Eric T. Ahrens,* and Angelique Y. Louie*

Cite This: *ACS Nanosci. Au* 2022, 2, 102−110

Read Online

ACCESS | Metrics & More | Article Recommendations | SI Supporting Information

ABSTRACT: We describe an *in vivo* imaging probe platform that is readily modifiable to accommodate binding of different molecular targeting moieties and payloads for multimodal image generation. In this work, we demonstrate the utility of perfluorocarbon (PFC) nanoemulsions incorporating dibenzocyclooctyne (DBCO) by enabling post-emulsification functionalization via a click reaction with azide-containing ligands. The addition of DBCO-lipid to the surfactant in PFC nanoemulsions did not affect nanoemulsion size or nanoemulsion stability. As proof-of-concept, fluorescent dye-azides were conjugated to PFC nanoemulsions, demonstrating the feasibility of functionalization the by click reaction. Uptake of the fluorescent PFC by macrophages was demonstrated both *in vitro* in cultured macrophages and *in situ* in an acute inflammation mouse model, where fluorescence imaging and ^{1}H/^{19}F magnetic resonance imaging (MRI) were used for *in vivo* detection. Overall, these data demonstrate the potential of PFC nanoemulsions incorporating DBCO as a versatile platform for generating functionalized probes.

KEYWORDS: *Fluorine MRI, perfluorocarbon, click chemistry, cell targeting, cell tracking*
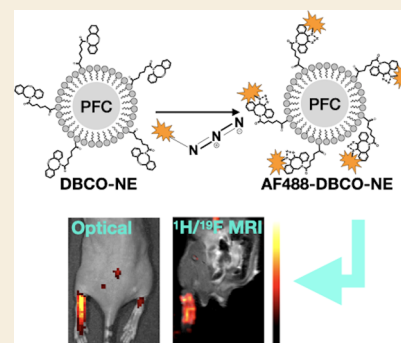
INTRODUCTION

Magnetic resonance imaging (MRI) is a powerful technique for noninvasively visualizing soft-tissue anatomical morphology at high-resolution and is a common clinical diagnostic tool. *In vivo* cell tracking is a relatively new use for MRI that is making inroads toward clinical use.[1,2] The ^{19}F nucleus is an attractive tracer probe for *in vivo* "hot-spot" MRI due to the relatively high sensitivity, which is comparable to ^{1}H nuclei, and its low background in biological tissues compared to typical relaxation-weighted imaging.[3,4] Coincident ^{1}H MRI provides the anatomical context for image interpretation.

Perfluorocarbon (PFC) oils are a common fluorine tracer agent due to their F-dense composition, which affords high MRI sensitivity as well as overall biosafety.[5] The oils are most often formulated as nanoemulsions (NEs), which are colloidal suspensions of PFC droplets, stabilized using a surfactant. Cell uptake can be achieved by simple coincubation with cells of interest *ex vivo*, followed by delivery of the labeled cells to the subject. This approach is particularly useful for following the fate of emerging cytotherapies used to treat cancer.[6,7] Alternatively, NE is injected intravenously, and droplets are taken up by phagocytic cells of the reticuloendothelial system (RES), including macrophages at sites of inflammation. The utility of ^{19}F MRI has been demonstrated for imaging stem cells,[2,8] various immune cell subsets,[9,10] macrophage-associated inflammatory diseases, and regenerative medicine.[11,12] Overall, ^{19}F MRI detection is feasible when 10^3−10^5 cells locally accumulate to generate an image hot-spot.[13]

Our goal is to adorn NE with ligands bearing affinity for distinct cellular biomarkers as well as moieties for multimodal imaging. Imaging probes harboring a variety of ligand types such as peptides, antibodies, polymers, dyes, and chelates are of the greatest interest.[14,15] Strategies for NE surface functionalization have been reported using two distinct methods, including pre- and post-emulsification approaches.[16] Pre-emulsification techniques rely on ligand conjugation before the high-pressure, homogenization process (i.e., microfluidization) to form the stabilized NE.[17−19] While this method may be simplistic to implement, ligands must be robust enough to withstand the extreme shear forces imposed by the homogenization. In the post-emulsification approach, the ligand is conjugated to the surface after the emulsification process is complete.[3] This requires chemical modification of the surface of the droplets to introduce functional groups, e.g., amine, carboxyl, or sulfhydryl. Prior efforts[20] have employed sulfhydryl-based linker chemistry for NE conjugation by the formation of covalent thioether bonds between maleimide and cysteine groups without the need for metal catalysts. However, there are reported limitations with this strategy, such as the
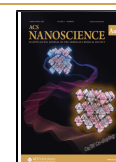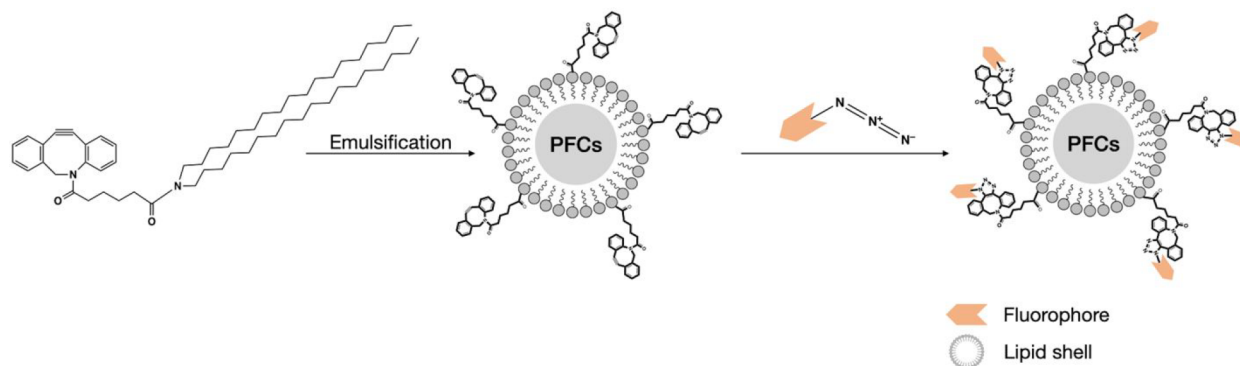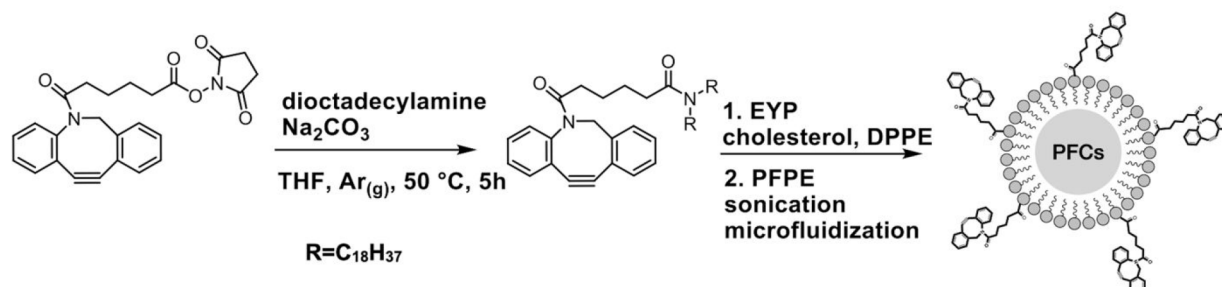
Figure 1. Summary of the strategy used to functionalize NE for ligand conjugation.

Scheme 1. Synthesis of DBCO-PFC NE

maleimide-linked products being sensitive to hydrolysis, instability *in vivo*,[21] and the chemistry optimally requiring an inert atmosphere.[22] Functionalized NEs bind successfully to targets and are stable in proper storage conditions.[16,23] However, current methods for preparing surface-functionalized nanoemulsions are time intensive and require a multistep process.

To streamline functionalization, we present a novel methodology for efficient moiety attachment using copper-free click chemistry and click-ready NE. We demonstrate a strategy commonly known as strain-promoted alkyne–azide cyclo-addition (SPAAC) to facilitate NE conjugation (Figure 1). Desirably, this click chemistry occurs in mild reaction conditions and has low potential for cross-reactivity.[24] SPAAC has been used successfully for a variety of biological applications, such as radioisotope labeling, live-cell imaging, and surface modification but has not been adapted for use with nanoemulsions.[25−30] Here, we modify the dibenzocyclooctyne succinimidyl ester (DBCO-NHS ester) linker with a lipid tail, dioctadecylamine, to facilitate incorporation to the nano-emulsion surfactant coat and present the reactive cyclooctyne on the surface of the nanoemulsion. Overall, these NE compositions can be used with a library of surface attachable ligand/moieties for targeting, imaging, and cargo delivery. This ability greatly enhances the utility of perfluorocarbon nano-emulsions as a flexible tool for multimodal imaging.

RESULTS AND DISCUSSION

Characterization and Kinetic Stability of Click-Ready DBCO-NE

The preparation of unfunctionalized PFC NE (control NE) is well described and characterized for its pharmacokinetic properties and shows good stability and biocompatibility;[31] thus, the synthesis of DBCO-NE builds on this prior work.

Dioctadecylamine serves as a vehicle for lipid insertion into the nanoemulsion formulation.[32] Perfluoropolyether (PFPE) oil was selected for the PFC core of the NE, as it displays a single major ^{19}F resonance and a short T1 relaxation time around 400 ms at 9.4 T.[33−35]

The DBCO-NHS reaction with dioctadecylamine produced the amide-linked product in 90% yield (Scheme 1). The DBCO-lipid product was validated by ^1H NMR and mass spectrometry (Figure S1). Chromatographically purified DBCO-lipid was used for subsequent NE synthesis. The DBCO-lipid was incorporated into the lipid formulation at various mol %'s in relationship to the total moles of egg yolk phospholipid (EYP) content. Table 1 summarizes size and

Table 1. Hydrodynamic Size Diameters and PDI Values of DBCO-NE

NE types	hydrodynamic diameter (nm)	PDI
PFC NE (control NE)	165.5 ± 2.5	0.109 ± 0.020
0.2 mol % DBCO-NE	162.5 ± 0.5	0.124 ± 0.018
0.5 mol % DBCO-NE	166.7 ± 2.7	0.134 ± 0.013
1 mol % DBCO-NE	168.2 ± 1.3	0.127 ± 0.023
5 mol % DBCO-NE	167.8 ± 1.7	0.134 ± 0.003
X^2	0.1	0.021

polydispersity index (PDI) for unmodified PFC NE and 4 different mol % of DBCO added (0.2, 0.5, 1.0, and 5.0 mol % DBCO). There are no significant changes with increasing DBCO concentration for both mean droplet size and PDI, indicating that the addition of the DBCO-lipid does not perturb PFC NE size or distribution (Table 1). The minimum DBCO introduced was based on previous studies showing that 0.5 mol % of ligand attached to PFC NE provided optimal uptake.[17]
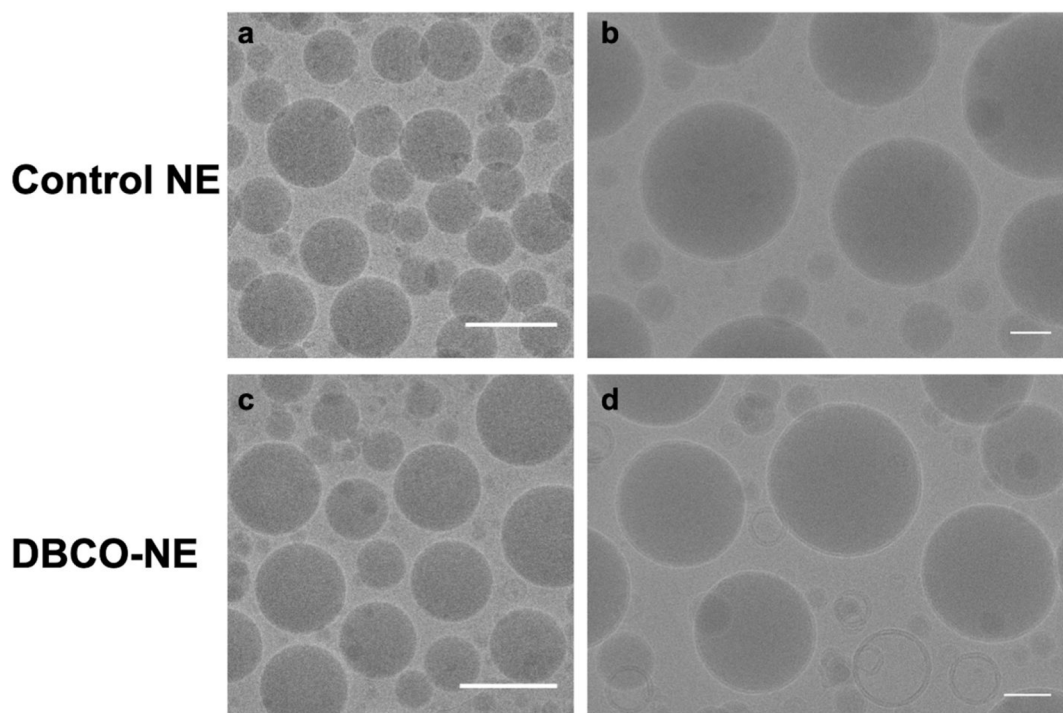
Figure 2. Representative cryoEM images for control NE and DBCO-NE. Control NE (a) and 5 mol % DBCO-NE (c) cryoEM images were obtained at 11 000× magnification (scale bar = 200 nm). Control NE (b) and 5 mol % DBCO-NE (d) cryoEM images were obtained at 45 000× magnification (scale bar = 50 nm).
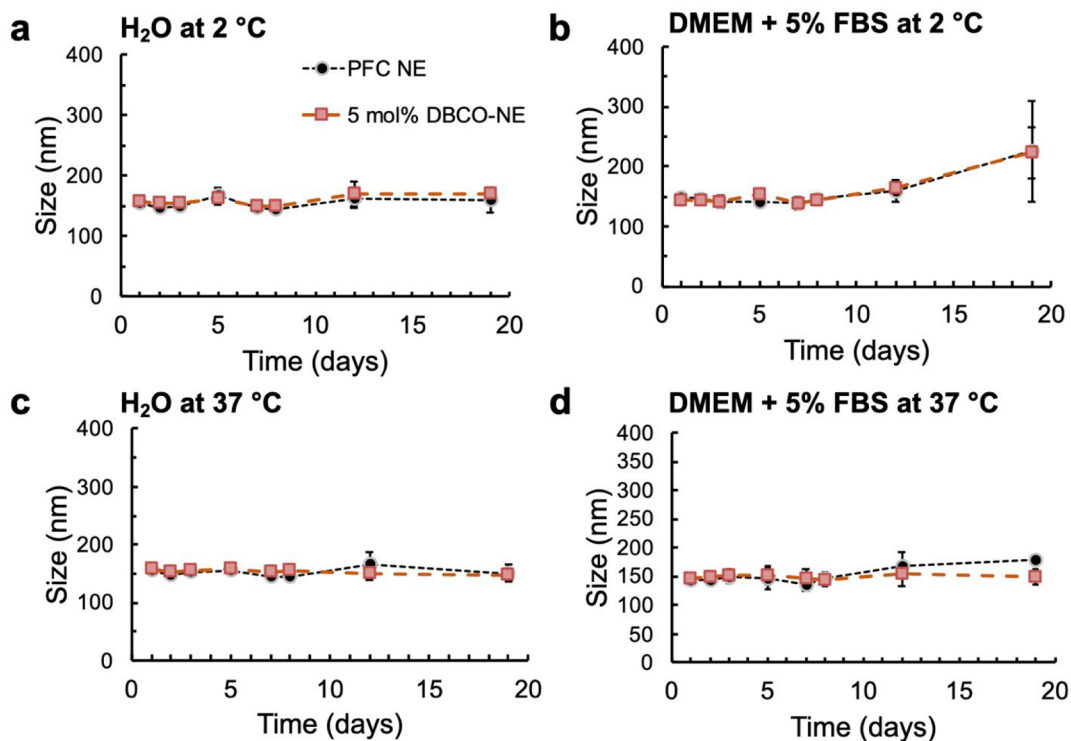

Figure 3. DLS results for droplet size changes over 19 days for PFC NE (control NE) and 5 mol % DBCO-NE in pure water or proteinaceous buffer at various temperatures. Error bars reflect the standard deviation for $n = 3$. (a) No size differences were found for control NE and DBCO-NE ($p = 0.32, 0.035$). (b) Size increased over time for both NE types stored in DMEM with 5% FBS at 2 °C ($p = 8.99 \times 10^{-6}$ for DBCO-NE, $p = 9.42 \times 10^{-6}$ for control NE). (c) No size changes are observed for either NE type in water at 37 °C ($p = 0.105$ for DBCO NE, $p = 0.73$ for control NE). (d) The size change over time was not significant for DBCO NE in DMEM with 5% FBS at 37 °C ($p = 0.799$), but the size of the control NE increased over time ($p = 2.87 \times 10^{-6}$). Size changes over time were considered significant for p values < 0.01.

Five mol % DBCO NE was chosen to represent the morphology of DBCO conjugated PFC NE. Figure 2 shows the representative cryoEM images for control NE and 5 mol % DBCO-NE. As expected, the size of the droplets is slightly smaller compared to the hydrodynamic sizes measured by DLS for both control NE and 5 mol % DBCO-NE. The lipid layer of the nanoemulsion is clearly shown as a 3.5 ± 0.3 nm layer on the surface of the droplet in 45 000× magnified images (Figure 2b,d).

A number of processes can affect the stability of NE over time, in solution, including Ostwald's ripening, perfluorocarbons volatility, and lipid oxidation.[36] To observe NE stability and confirm that the addition of DBCO-lipid does not adversely affect stability, we studied NE and DBCO-NE under a variety of potential storage conditions in solution. Incubation conditions were selected to simulate the effects of long-term storage under refrigeration or a simulated *in vivo* environment. Nanoemulsions were stored at 2 or 37 °C in pure water or Dulbecco's Modified Eagle Medium (DMEM) with 5% fetal bovine serum (FBS) as shown in Figure 3. The size of control NE and DBCO-NE increased significantly over time at 2 °C in DMEM media with 5% FBS (p value = p = 9.42×10^{-6}, 8.99×10^{-6}). No significant size changes were found for control NE and DBCO-NE at 2 °C in water (p = 0.32, 0.035). This is not unexpected as storage in proteinaceous media can result in coating of the nanoemulsion droplets with protein, effectively increasing the hydrodynamic size over time. At 37 °C in water and in DMEM with 5% FBS storage conditions, no significant size changes over time were found for DBCO-NE (p value = 0.105 and 0.799, respectively). The size of control NE increased over time under 37 °C in DMEM media with 5% FBS (p = 2.87×10^{-6}), but no significant size changes were found for control NE under 37 °C in water (p = 0.73). At 37 °C in DMEM media with 5% FBS, the size change over time for control NE was larger than the size change over time for DBCO-NE (Figure 3d). The sizes of control NE and DBCO-NE were at least stable for 3 days, which is suitable for *in vitro* and *in vivo* macrophage labeling and imaging. Statistical analysis was done with a linear mixed model from the lme4 package and followed by a z test of the model estimated change over time with the emmeans package in R. Size changes over time were considered significant for p values < 0.01.

Characterization of Clicking Efficiency of DBCO-NE

Additionally, we examined whether varying mol % DBCO content impacted ligand coupling efficiencies. To explore the conjugating capacity of the NE droplets and efficiency of the click reaction, DBCO-PFC NEs were reacted with Alexa Fluor 488 azide as a test ligand ($\lambda_{ex/em}$ = 494/517 nm, AF488, Click Chemistry Tools, Scottsdale, AZ), and coupling was validated by absorbance spectroscopy. Bound and unbound ligands are distinguishable via elution profiles through a size-exclusion separation column (Sephadex G50, Sigma-Aldrich, Milwaukee, MI). Larger PFC NE droplets elute faster (Figure 4a, fractions 1−10), whereas free AF488 displays slow elution (Figure 4a, fractions 15−30). The range of AF488 used for all emulsions was 50−200 μM in order to assess changes in binding capacity over the mol % DBCO range. As summarized in Figure 4a, the absorbance signal for bound AF488 (fractions 4−6) appears with a minimum of 0.5 mol % DBCO and increases in amplitude as the mol % DBCO increases (Figure 4a, trace C), while the peak for unbound AF488 (fractions 23−26) decreases. As expected, the higher mol % DBCO concen-
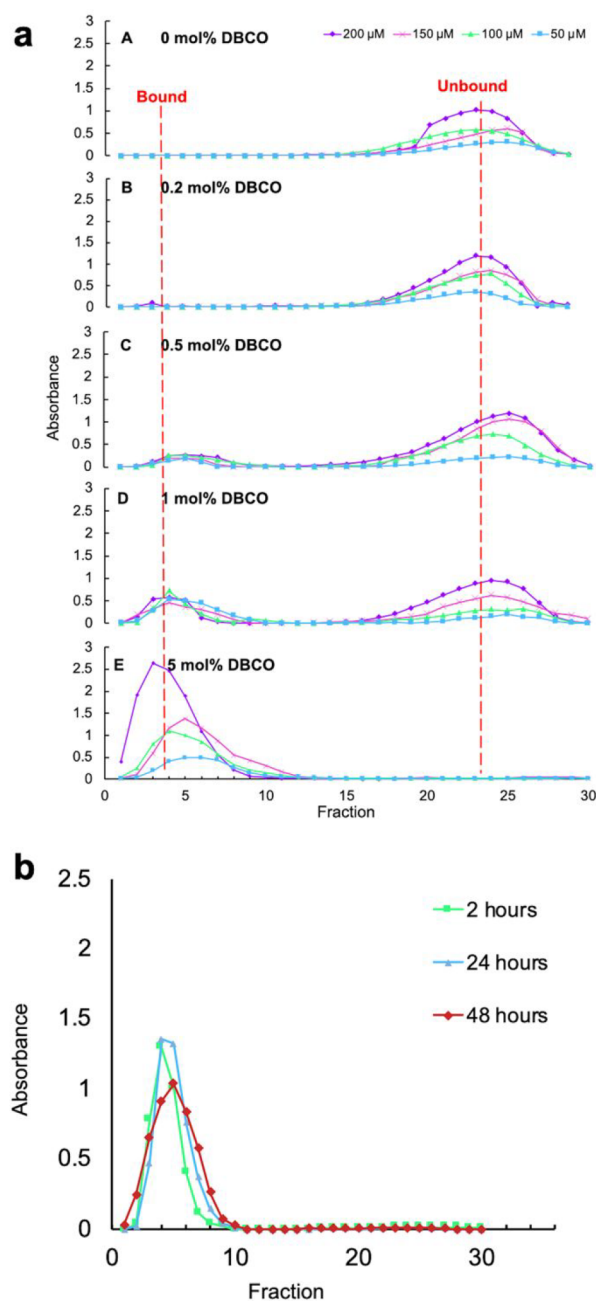

Figure 4. Clicking efficiency profile for DBCO-NE. (a) Elution profiles of DBCO-NE reacted with AF488 azide separated by a size-exclusion column. AF488 clicked to DBCO-NE; AF488-DBCO-NE elutes more rapidly in fractions 1−10 while unbound AF488 elutes in 15−30. (b) Elution profile of 5 mol % DBCO-NE reacted with 130 μM AF488 azide for three different reaction times at room temperature (n = 3 per time condition). No significant difference in absorbance, a measure of the amount of AF488 clicked to 5 mol % DBCO-NE, was observed.

trations (Figure 4a, traces D, E) show an increase in AF488 conjugation effectiveness with 5 mol % DBCO displaying complete ligand binding. The observed plateau in bound ligand suggests that the binding capacity of the DBCO-NE has been reached or exceeded. We further evaluated optimal reaction times using 5 mol % DBCO-NE. The click reaction was assayed at 2, 24, and 48 h. As shown in Figure 4b, the reaction appears to saturate by 2 h with no significant changes thereafter (p value = 0.456).
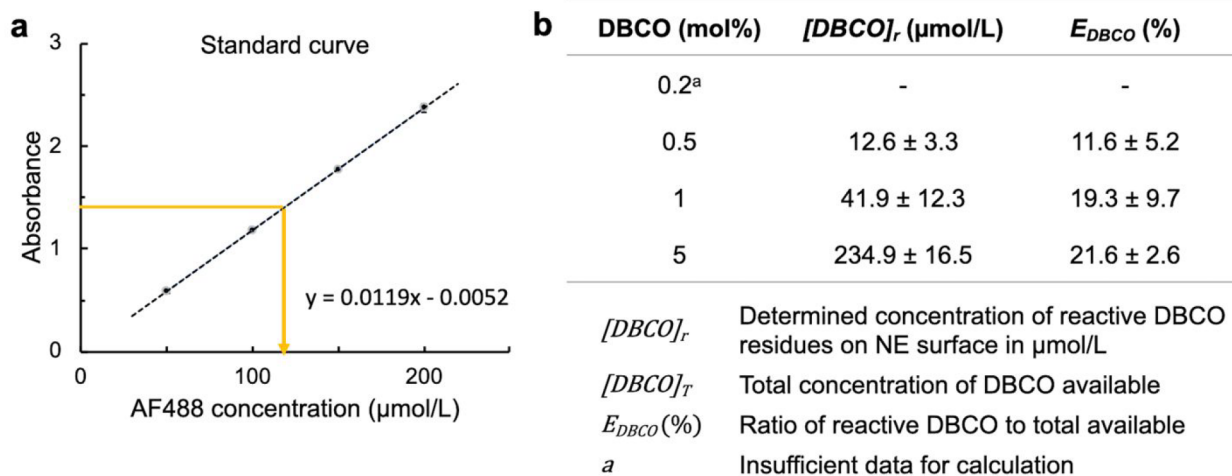
Figure 5. DBCO-NE click efficiency evaluation. (a) AF488-DBCO-NE absorbance standard curve, which was used to determine reactive DBCO concentration on NE. (b) Summary of relative clicking efficiency for DBCO-NE.

Relative clicking efficiency, E_{DBCO}, was defined as the ratio of the number of reacted DBCO residues ($[DBCO]_r$) compared to the total added DBCO ($[DBCO]_T$, eq 1). We collected bound fractions (1−10), and $[AF488]$ present on the saturated DBCO-NE ($n = 4$) was quantified by measuring absorbance on a plate reader (Infinite M200PRO, Tecan, Morrisville, NC) aided by the AF488 standard curve (Figure 5). The 0.2 mol % DBCO sample had no detectable absorbance. Figure 5 shows statistically significant changes in $[DBCO]_r$ with a 3.3-fold increase from 0.5 to 1 mol % and a 5.6-fold increase from 1 to 5 mol %. The highest efficiency of the click reaction occurred for 5 mol % DBCO with $21.6 \pm 2.6\%$ reacted DBCO relative to total DBCO added as starting material. The 5 mol % DBCO-NE was used for all *in vitro* and *in vivo* assays described below.

$$E_{DBCO} = \frac{[DBCO]_r}{[DBCO]_T} \times 100\%$$

(1)

Cytotoxicity of Conjugated and Unconjugated DBCO-NE

Preliminary cytotoxicity of DBCO NE was assessed on macrophages (RAW 264.7 cells, ATCC, Manassas, VA) and compared to treatment with control NE (PFC NE) and AF488-DBCO-NE (fluorescent dye click-conjugated NE). One million cells per condition were incubated overnight at 37 °C with ascending doses ranging from 2 to 10 mg/mL PFPE in DBCO-NE and AF488-DBCO-NE ($n = 3$). Viability was assayed by trypan blue staining. As shown in Figure 6, no statistically significant differences were found for cell viability between control NE, DBCO-NE, or AF488-DBCO-NE within same incubated concentration. However, when RAW 264.7 cells were treated with 8 mg/mL (PFPE concentration) DBCO-NE, cell viability decreased ($p = 0.0018$), and cell viability decreased when treated with 10 mg/mL (PFPE concentration) of control NE, DBCO-NE, or AF488-DBCO-NE ($p = 0.00059, 7.74 \times 10^{-5}, 0.00037$, respectively). Cell viabilities are above 80% under all treatment conditions. The statistical analysis was done by using a generalized linear model ANOVA from the lme package, and p values are corrected for multiple comparisons within a given outcome with the Bonferroni-Holm correction for 30 tests in R.
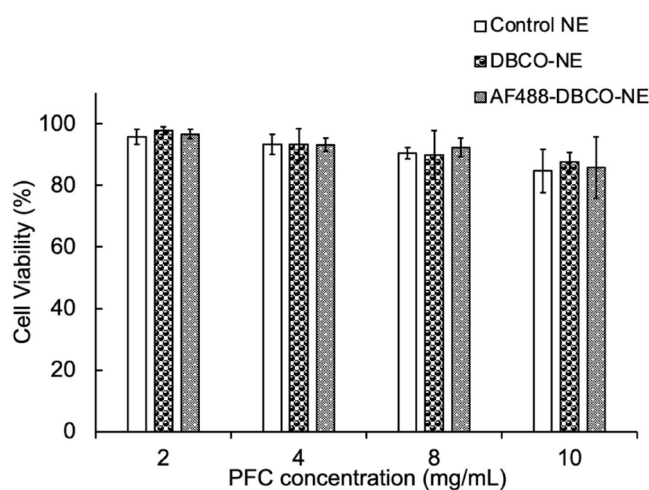

Figure 6. Cytotoxicity assays with click NE. RAW 264.7 macrophages were incubated with various concentrations of click-ready DBCO-NE or fluorescent click conjugated AF488-DBCO-NE ($n = 3$), and no significant differences compared to control NE treated cells were observed. Cell viability decreased when treated with 10 mg/mL PFPE in control NE and AF488-DBCO-NE ($p = 0.00059, 0.00037$). DBCO-NE treated cells showed lower viability when treated with 8 mg/mL or a higher concentration of PFPE ($p = 0.0018, 7.74 \times 10^{-5}$). Cell viability was above 80% under all conditions.

In Vivo Optical Imaging and ¹⁹F MRI of AF488-DBCO-NE

We performed proof-of-concept rodent experiments using whole-body fluorescence imaging and ¹⁹F MRI to confirm probe stability and detectability *in vivo*. All animal experiments followed protocols that were approved by University of California San Diego's Institutional Animal Care and Use Committee. We used an acute inflammation model in female CD-1 mice.[37] 1% carrageenan solution in saline was injected subcutaneously into the right hind footpad ($n = 3$, ICR CD-1, Envigo, Indianapolis, IN) to induce a progressive edema within 4 h.[38,39] On the same day, AF488-DBCO-NE (0.3 mL, 112 mg/mL, 324 μM AF488/DBCO) was injected via tail vein. The clearance kinetics of PFC NE and the ¹⁹F MRI signal are well described in the literature,[40,41] and the inflammatory lesion in the paw edema model subsides in 2−3 days;[42] thus, the 24 h post-injection imaging time point was chosen. At 24 h
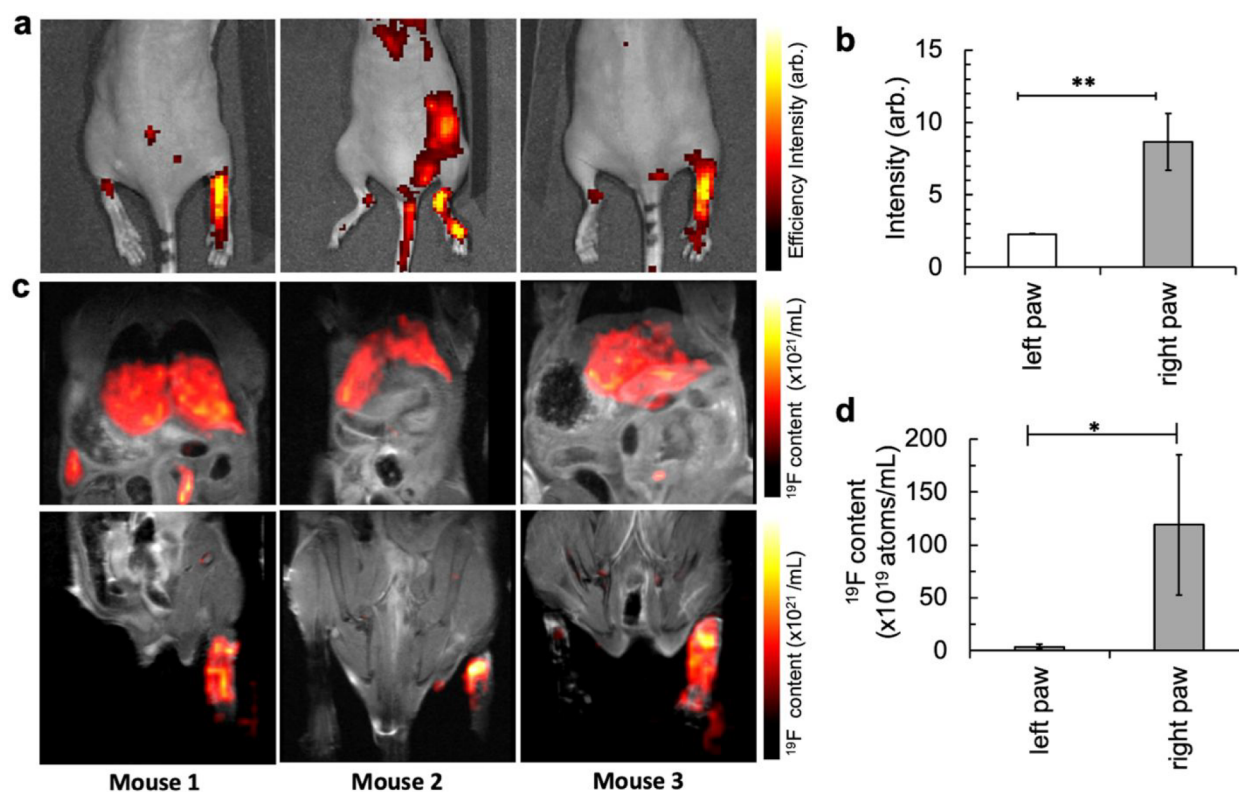
Figure 7. Localization of *in situ* AF488-DBCO-NE labeled immune cells in a mouse model of acute inflammation. (a) *In vivo* fluorescence images of hindquarters of female CD-1 mice 24 h after tail vein injection of AF488-DBCO-NE injection ($n = 3$). Fluorescence intensity is presented on a "hot-iron" color scale bar. The right paw and leg display signal hot-spots, indicative of AF488-DBCO-NE localization to the site of inflammation. (b) Quantification of the fluorescence intensity confirms a higher signal in the inflamed right paw. (c) Composite $^1H/^{19}F$ MRI of torso and hindquarters (upper and lower panels, respectively) showing the ^{19}F signal in hot-iron scale with ^1H in grayscale. The signal is evident in the inflamed right paw and in the liver (part of the RES clearance pathway). (d) Quantification of ^{19}F content of hind paws using region of interest volumetric analysis. The differences were considered significant with p values of * < 0.05 and ** < 0.01 as shown.
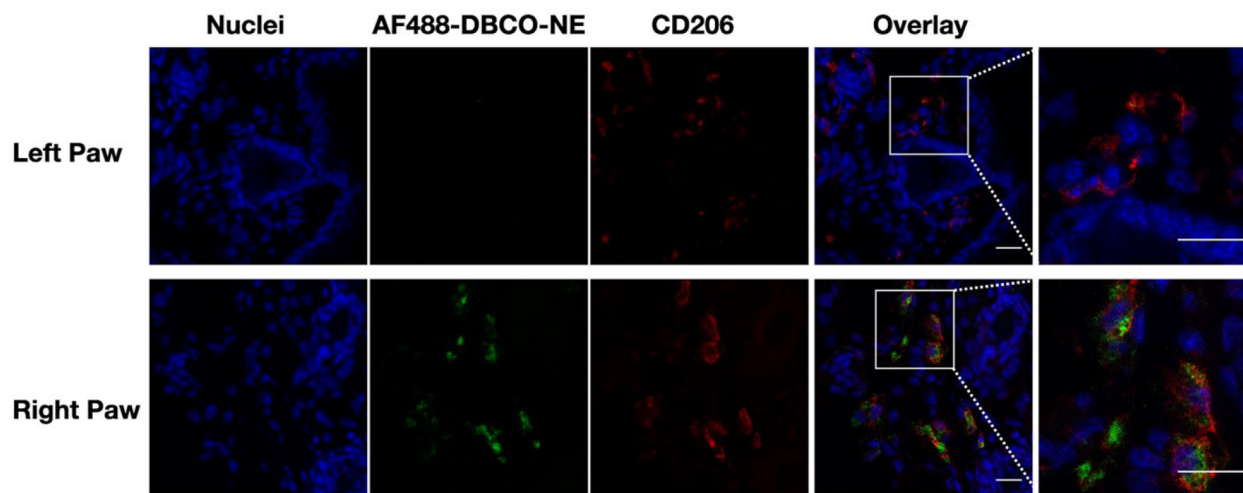

Figure 8. Confocal images of mouse paw in acute inflammation model showing *in situ* macrophage labeling with AF488-DBCO-NE. Overlays of nuclei (blue), mannose receptor (red,) and AF488-DBCO-NE (green) are shown. The control left paw slice displays minimal macrophage presence and low levels of AF488-DBCO-NE. In contrast, prominent intracellular localization of AF488-DBCO-NE in macrophages in the inflamed right paw is observed. Scale bars = 20 μm.

post-injection, anesthetized mice were imaged *in vivo*. Figure 7a shows a characteristic example of whole-body fluorescent images (IVIS, PerkinElmer, Waltham, MA), which display an intense hot-spot in the injected right paw compared to the contralateral control paw with a significant 4-fold higher emission (Figure 6b, $p = 0.009$, t test). In the same animals, ^{19}F MRI (Figure 7c) also displays prominent hot-spots in the injected paw with 4-fold greater signal than the control side (Figure 7d, $p = 0.039$, t test). Notably, the liver signal, consistent with RES clearance of the probe, is prominent in the

^{19}F MRI but not in fluorescence due to tissue opacity blocking fluorescent signal. In the optical images, there are small fluorescence foci observed in the tail vein for mouse 2; this is presumably due to inflammation from the slight wounding that occurs during the tail vein injection. Combined, the whole-body fluorescence and ^{19}F MRI images demonstrate the feasibility of using AF488-DBCO-NE as a multimodal imaging agent. Moreover, the hot-spot coincidence between the two imaging methods suggests that the fluorescence and ^{19}F signal generating molecules remain stably complexed for at least 24 h *in vivo*.

To confirm that the AF488-DBCO-NE localized predominately to cells of macrophage phenotype, immunohistochemical (IHC) analysis was performed on the right and left paws using confocal microscopy. Necropsied paws were embedded in cryo-media, sectioned, then stained with antimannose receptor antibody (ab64693, Abcam, Waltham, MA), and detected using anti-rabbit IgG Alexa Fluor 647 antibody (A27040, ThermoFisher, Pittsburgh, PA). The cell nuclei were counterstained with Hoechst 33342. Co-localization between CD206$^+$ macrophages (red) and AF488-DBCO-NE (green) is observed in the right paw only (Figure 8). These observations support the view that the probe preferentially localizes in the inflamed right paw but not in the contralateral control, consistent with the *in vivo* imaging results.

CONCLUSIONS

To summarize, we report a novel bioconjugation method for PFC NE that uses copper-free click chemistry to attach fluorescent dye, and we demonstrate successful clicking of a fluorescent azide as proof-of-concept. Overall, the click modification shows excellent reactivity in mild conditions in water at room temperature. Approximately 21% of the introduced DBCO was available for the click reaction. Potentially, the reaction efficiency could be increased by extending the DBCO group further from the surface to improve accessibility for click reactions. The clickable AF488-DBCO-NE formulation, suitable for intravenous injection and *in situ* macrophage labeling, successfully displays dual-mode, coincident fluorescence, and ^{19}F MRI signals in a mouse model of acute inflammation.

Click-ready DBCO-NE has the potential to streamline preparations of PFC NE for molecular imaging. The rapid click reaction and ability to click post-emulsification enable nanoemulsions to be used in applications requiring ligands that are sensitive to harsh temperature and pressure conditions experienced during emulsification procedures, such as antibodies, peptides, proteins. Moreover, coupling of a variety of azide-modified ligands could facilitate targeting to desired cell phenotypes as well as therapeutic cargo delivery. The availability of many commercial, azide-functionalized ligands offers a convenient resource for biological laboratories to readily modify click-ready NE for customized applications, for example, using cancer biomarkers to track distant metastases or inflammation biomarkers to visualize a localized infection. Also, ^{19}F MRI with different PFC oils has the potential to image multiple targets simultaneously, for example, by using two different PFC oils with different chemical shifts, which can be resolved using ^{19}F MRI.

ASSOCIATED CONTENT

SI Supporting Information

The Supporting Information is available free of charge at https://pubs.acs.org/doi/10.1021/acsnanoscienceau.1c00016.

Method section (PDF)

Video file showing 360° views of the mouse 3, in Figure 7, with the signal corresponding to sciatic and popliteal lymph nodes as well as the right paw (AVI), and reference tube used for quantification (located below ventral side of animal)

AUTHOR INFORMATION

Corresponding Authors

Angelique Y. Louie − *Chemistry Graduate Group, University of California Davis, Davis, California 95616, United States; Department of Biomedical Engineering, University of California Davis, Davis, California 95616, United States;* orcid.org/0000-0001-6610-5356; Email: aylouie@ucdavis.edu

Eric T. Ahrens − *Department of Radiology, University of California, San Diego, La Jolla, California 92093, United States;* orcid.org/0000-0001-6131-9304; Email: eahrens@health.ucsd.edu

Authors

Adam S. Perez − *Chemistry Graduate Group, University of California Davis, Davis, California 95616, United States*

Junhan Zhou − *Chemistry Graduate Group, University of California Davis, Davis, California 95616, United States;* orcid.org/0000-0001-8902-7514

Benjamin Leach − *Department of Radiology, University of California, San Diego, La Jolla, California 92093, United States*

Hongyan Xu − *Department of Radiology, University of California, San Diego, La Jolla, California 92093, United States*

Deanne Lister − *Department of Radiology, University of California, San Diego, La Jolla, California 92093, United States*

Stephen R. Adams − *Department of Pharmacology, University of California, San Diego, La Jolla, California 92093, United States;* orcid.org/0000-0002-4725-2091

Complete contact information is available at:
https://pubs.acs.org/10.1021/acsnanoscienceau.1c00016

Author Contributions

$^{\nabla}$A.S.P. and J.Z. contributed equally to this work.

Notes

The authors declare the following competing financial interest(s): E.T.A. is a founder and shareholder of Celsense, Inc. The other authors have nothing to disclose.

■ REFERENCES

(1) Ruiz-Cabello, J.; Barnett, B. P.; Bottomley, P. A.; Bulte, J. W. M. Fluorine (19F) MRS and MRI in Biomedicine. *NMR Biomed.* **2011**, *24* (2), 114−129.

(2) Janjic, J. M.; Ahrens, E. T. Fluorine-Containing Nanoemulsions for MRI Cell Tracking. *Wiley Interdiscip. Rev. Nanomedicine Nanobiotechnology* **2009**, *1* (5), 492−501.

(3) Srinivas, M.; Morel, P. A.; Ernst, L. A.; Laidlaw, D. H.; Ahrens, E. T. Fluorine-19 MRI for Visualization and Quantification of Cell Migration in a Diabetes Model. *Magn. Reson. Med.* **2007**, *58* (4), 725−734.

(4) Barrow, M.; Taylor, A.; Murray, P.; Rosseinsky, M. J.; Adams, D. J. Design Considerations for the Synthesis of Polymer Coated Iron Oxide Nanoparticles for Stem Cell Labelling and Tracking Using MRI. *Chem. Soc. Rev.* **2015**, *44*, 6733−6748.

(5) Cantow, M.; Larrabee, R.; Barrall, E.; Butner, R.; Cotts, P.; Levy, F.; Ting, T. Molecular Weights and Molecular Dimensions of Perfluoropolyether Fluids. *Makromol. Chem.* **1986**, *187* (10), 2475−2481.

(6) Frank, J. A.; Anderson, S. A.; Kalsih, H.; Jordan, E. K.; Lewis, B. K.; Yocum, G. T.; Arbab, A. S. Methods for Magnetically Labeling Stem and Other Cells for Detection by in Vivo Magnetic Resonance Imaging. *Cytotherapy* **2004**, *6* (6), 621−625.

(7) Boehm-Sturm, P.; Mengler, L.; Wecker, S.; Hoehn, M.; Kallur, T. In Vivo Tracking of Human Neural Stem Cells with 19F Magnetic Resonance Imaging. *PLoS One* **2011**, *6* (12), No. e29040.

(8) Gaudet, J. M.; Ribot, E. J.; Chen, Y.; Gilbert, K. M.; Foster, P. J. Tracking the Fate of Stem Cell Implants with Fluorine-19 MRI. *PLoS One* **2015**, *10* (3), e0118544.

(9) Helfer, B. M.; Balducci, A.; Nelson, A. D.; Janjic, J. M.; Gil, R. R.; Kalinski, P.; De Vries, I. J. M.; Ahrens, E. T.; Mailliard, R. B. Functional Assessment of Human Dendritic Cells Labeled for in Vivo 19F Magnetic Resonance Imaging Cell Tracking. *Cytotherapy* **2010**, *12* (2), 238−250.

(10) Nöth, U.; Morrissey, S. P.; Deichmann, R.; Jung, S.; Adolf, H.; Haase, A.; Lutz, J. Perfluoro-15-Crown-5-Ether Labelled Macrophages in Adoptive Transfer Experimental Allergic Encephalomyelitis, Artificial Cells. *Blood Substitutes, Biotechnol.* **1997**, *25* (3), 243−254.

(11) Edmundson, M.; Thanh, N. T. K.; Song, B. Nanoparticles Based Stem Cell Tracking in Regenerative Medicine. *Theranostics* **2013**, *3* (8), 573−582.

(12) Scarfe, L.; Brillant, N.; Kumar, J. D.; Ali, N.; Alrumayh, A.; Amali, M.; Barbellion, S.; Jones, V.; Niemeijer, M.; Potdevin, S.; et al. Preclinical Imaging Methods for Assessing the Safety and Efficacy of Regenerative Medicine Therapies. *npj Regen. Med.* **2017**, *2*, 28.

(13) Gálisová, A.; Herynek, V.; Swider, E.; Sticová, E.; Pátiková, A.; Kosinová, L.; Kříž, J.; Hájek, M.; Srinivas, M.; Jirák, D. A Trimodal Imaging Platform for Tracking Viable Transplanted Pancreatic Islets In Vivo: F-19 MR, Fluorescence, and Bioluminescence Imaging. *Mol. Imaging Biol.* **2019**, *21* (3), 454−464.

(14) Riaz, M.; Riaz, M.; Zhang, X.; Lin, C.; Wong, K.; Chen, X.; Zhang, G.; Lu, A.; Yang, Z. Surface Functionalization and Targeting Strategies of Liposomes in Solid Tumor Therapy: A Review. *Int. J. Mol. Sci.* **2018**, *19* (1), 195.

(15) Veiseh, O.; Gunn, J. W.; Zhang, M. Design and Fabrication of Magnetic Nanoparticles for Targeted Drug Delivery and Imaging. *Adv. Drug Delivery Rev.* **2010**, *62*, 284−304.

(16) Krämer, W.; Grapentin, C.; Bouvain, P.; Temme, S.; Flögel, U.; Schubert, R. Rational Manufacturing of Functionalized, Long-Term Stable Perfluorocarbon-Nanoemulsions for Site-Specific 19F Magnetic Resonance Imaging. *Eur. J. Pharm. Biopharm.* **2019**, *142* (June), 114−122.

(17) Hingorani, D. V.; Chapelin, F.; Stares, E.; Adams, S. R.; Okada, H.; Ahrens, E. T. Cell Penetrating Peptide Functionalized Perfluorocarbon Nanoemulsions for Targeted Cell Labeling and Enhanced Fluorine-19 MRI Detection. *Magn. Reson. Med.* **2020**, *83* (3), 974−987.

(18) Janjic, J. M.; Srinivas, M.; Kadayakkara, D. K. K.; Ahrens, E. T. Self-Delivering Nanoemulsions for Dual Fluorine-19 MRI and Fluorescence Detection. *J. Am. Chem. Soc.* **2008**, *130* (9), 2832−2841.

(19) Li, S.; Wang, L.; Li, N.; Liu, Y.; Su, H. Combination Lung Cancer Chemotherapy: Design of a PH-Sensitive Transferrin-PEG-Hz-Lipid Conjugate for the Co-Delivery of Docetaxel and Baicalin. *Biomed. Pharmacother.* **2017**, *95* (27), 548−555.

(20) Hingorani, D. V.; Chapelin, F.; Stares, E.; Adams, S. R.; Okada, H.; Ahrens, E. T. Cell Penetrating Peptide Functionalized Perfluorocarbon Nanoemulsions for Targeted Cell Labeling and Enhanced Fluorine□19 MRI Detection. *Magn. Reson. Med.* **2020**, *83* (3), 974−987.

(21) Szijj, P. A.; Bahou, C.; Chudasama, V. Minireview: Addressing the Retro-Michael Instability of Maleimide Bioconjugates. *Drug Discovery Today: Technol.* **2018**, *30*, 27−34.

(22) Butler, P. J.; Harris, J. I.; Hartley, B. S.; Lebeman, R. The Use of Maleic Anhydride for the Reversible Blocking of Amino Groups in Polypeptide Chains. *Biochem. J.* **1969**, *112* (5), 679−689.

(23) Ning, X.; Guo, J.; Wolfert, M. A.; Boons, G.-J. Visualizing Metabolically-Labeled Glycoconjugates of Living Cells by Copper-Free and Fast Huisgen Cycloadditions. *Angew. Chem., Int. Ed.* **2008**, *47*, 2253−2255.

(24) Liu, F.; Liang, Y.; Houk, K. N. Bioorthogonal Cycloadditions: Computational Analysis with the Distortion/Interaction Model and Predictions of Reactivities. *Acc. Chem. Res.* **2017**, *50* (9), 2297−2308.

(25) Mushtaq, S.; Yun, S. J.; Jeon, J. Recent Advances in Bioorthogonal Click Chemistry for Efficient Synthesis of Radiotracers and Radiopharmaceuticals. *Molecules* **2019**, *24* (19), 3567.

(26) Lee, S. B.; Kim, H. L.; Jeong, H.-J.; Lim, S. T.; Sohn, M.-H.; Kim, D. W. Mesoporous Silica Nanoparticle Pretargeting for PET Imaging Based on a Rapid Bioorthogonal Reaction in a Living Body. *Angew. Chem.* **2013**, *125* (40), 10743−10746.

(27) Jewett, J. C.; Sletten, E. M.; Bertozzi, C. R. Rapid Cu-Free Click Chemistry with Readily Synthesized Biarylazacyclooctynones. *J. Am. Chem. Soc.* **2010**, *132* (11), 3688−3690.

(28) Devaraj, N. K.; Upadhyay, R.; Haun, J. B.; Hilderbrand, S. A.; Weissleder, R. Fast and Sensitive Pretargeted Labeling of Cancer Cells through a Tetrazine/Trans-Cyclooctene Cycloaddition. *Angew. Chem., Int. Ed.* **2009**, *48* (38), 7013−7016.

(29) Laughlin, S. T.; Baskin, J. M.; Amacher, S. L.; Bertozzi, C. R. In Vivo Imaging of Membrane-Associated Glycans in Developing Zebrafish. *Science (Washington, DC, U. S.)* **2008**, *320* (5876), 664−667.

(30) Dommerholt, J.; Rutjes, F. P. J. T.; van Delft, F. L. Strain-Promoted 1,3-Dipolar Cycloaddition of Cycloalkynes and Organic Azides. *In Topics in Current Chemistry* **2016**, *374*, 57−76.

(31) Jahromi, A. H.; Wang, C.; Adams, S. R.; Zhu, W.; Narsinh, K.; Xu, H.; Gray, D. L.; Tsien, R. Y.; Ahrens, E. T. Fluorous-Soluble Metal Chelate for Sensitive Fluorine-19 Magnetic Resonance Imaging Nanoemulsion Probes. *ACS Nano* **2019**, *13* (1), 143−151.

(32) Flores, A.; Ize, P.; Ramos, S.; Castillo, R. The Dioctadecylamine Monolayer: Textures, Phase Transitions, and Dendritic Growth. *J. Chem. Phys.* **2003**, *119* (11), 5644−5653.

(33) Zhang, C.; Moonshi, S. S.; Han, Y.; Puttick, S.; Peng, H.; Magoling, B. J. A.; Reid, J. C.; Bernardi, S.; Searles, D. J.; Král, P.; et al. PFPE-Based Polymeric 19F MRI Agents: A New Class of Contrast Agents with Outstanding Sensitivity. *Macromolecules* **2017**, *50* (15), 5953−5963.

(34) Helmer, K. G.; Han, S.; Sotak, C. H. On the Correlation between the Water Diffusion Coefficient and Oxygen Tension in RIF-1 Tumors. *NMR Biomed.* **1998**, *11* (3), 120−130.

(35) Dardzinski, B. J.; Sotak, C. H. Rapid Tissue Oxygen Tension Mapping Using19F Inversion-Recovery Echo-Planar Imaging of P Erfluoro-15 -Crown-5-Ether. *Magn. Reson. Med.* **1994**, *32* (1), 88−97.

(36) Rho, J.; Stares, E.; Adams, S. R.; Lister, D.; Leach, B.; Ahrens, E. T. Paramagnetic Fluorinated Nanoemulsions for in Vivo F-19 MRI. *Mol. Imaging Biol.* **2020**, *22* (3), 665−674.

(37) Whiteley, P. E.; Dalrymple, S. A. Models of Inflammation: Carrageenan-Induced Paw Edema in the Rat. In *Current Protocols in Pharmacology*; John Wiley & Sons, Inc.: Hoboken, NJ, USA, 2001; pp 5.4.1−5.4.3; DOI: 10.1002/0471141755.ph0504s00.

(38) Amdekar, S.; Roy, P.; Singh, V.; Kumar, A.; Singh, R.; Sharma, P. Anti-Inflammatory Activity of *Lactobacillus* on Carrageenan-Induced Paw Edema in Male Wistar Rats. *Int. J. Inflammation* **2012**, *2012*, 752015.

(39) Bohic, M.; Pattison, L. A.; Jhumka, Z. A.; Rossi, H.; Thackray, J. K.; Ricci, M.; Foster, W.; Arnold, J.; Mossazghi, N.; Yttri, E. A.; et al. Behavioral and Nociceptor States of Inflammatory Pain across Timescales in 2D and 3D. *bioRxiv* 2021, 2021.06.16.448689;.

(40) Staal, A. H. J.; Becker, K.; Tagit, O.; Koen van Riessen, N.; Koshkina, O.; Veltien, A.; Bouvain, P.; Cortenbach, K. R. G.; Scheenen, T.; Flögel, U.; et al. In Vivo Clearance of 19F MRI Imaging Nanocarriers Is Strongly Influenced by Nanoparticle Ultrastructure. *Biomaterials* **2020**, *261*, 120307.

(41) Janjic, J. M.; Ahrens, E. T. Fluorine-Containing Nanoemulsions for MRI Cell Tracking. *Wiley Interdiscip. Rev. Nanomedicine Nano-biotechnology* **2009**, *1* (5), 492−501.

(42) Posadas, I.; Bucci, M.; Roviezzo, F.; Rossi, A.; Parente, L.; Sautebin, L.; Cirino, G. Carrageenan-Induced Mouse Paw Oedema Is Biphasic, Age-Weight Dependent and Displays Differential Nitric Oxide Cyclooxygenase-2 Expression. *Br. J. Pharmacol.* **2004**, *142* (2), 331−338.